**Proceedings of the ASME 2021**
**International Mechanical Engineering Congress and Exposition**
**IMECE2021**
**November 1-5, 2021, Virtual, Online**

# IMECE2021-71315



# LEVERAGING VIBRATIONS AND GUIDED WAVES IN A HUMAN SKULL

**Eetu Kohtanen**
G. W. Woodruff School of Mechanical Engineering
Georgia Institute of Technology
Atlanta, Georgia

**Matteo Mazzotti, Massimo Ruzzene**
P. M. Rady Department of Mechanical Engineering
University of Colorado Boulder
Boulder, Colorado

**Alper Erturk**
G. W. Woodruff School of Mechanical Engineering
Georgia Institute of Technology
Atlanta, Georgia

## ABSTRACT

*This work is centered on high-fidelity modeling, analysis, and rigorous experiments of vibrations and guided (Lamb) waves in a human skull in two connected tracks: (1) layered modeling of the cranial bone structure (with cortical tables and diploë) and its vibration-based elastic parameter identification (and validation); (2) transcranial leaky Lamb wave characterization experiments and radiation analyses using the identified elastic parameters in a layered semi analytical finite element framework, followed by time transient simulations that consider the inner porosity as is. In the first track, non-contact vibration experiments are conducted to extract the first handful of modal frequencies in the auditory frequency regime, along with the associated damping ratios and mode shapes, of dry cranial bone segments extracted from the parietal and frontal regions of a human skull. Numerical models of the bone segments are built with a novel image reconstruction scheme that employs microcomputed tomographic scans to build a layered bone geometry with separate homogenized domains for the cortical tables and the diploë. These numerical models and the experimental modal frequencies are then used in an iterative parameter identification scheme that yields the cortical and diploic isotropic elastic moduli of each domain, whereas the corresponding densities are estimated using the total experimental mass and layer mass ratios obtained from the scans. With the identified elastic parameters, the average error between experimental and numerical modal frequencies is less than 1.5% and the modal assurance criterion values for most modes are above 0.90. Furthermore, the extracted parameters are in the range of the results reported in the literature. In the second track, the focus is placed on the subject of leaky Lamb waves, which has received growing attention as a promising alternative to conventional ultrasound techniques for transcranial transmission, especially to access the brain periphery. Experiments are conducted on the same cranial bone segment set for leaky Lamb wave excitation and radiation characterization. The degassed skull bone segments are used in submersed experiments with an ultrasonic transducer and needle hydrophone setup for radiation pressure field scanning. Elastic parameters obtained from the first track are used in guided wave dispersion simulations, and the radiation angles are accurately predicted using the aforementioned layered model in the presence of fluid loading. The dominant radiation angles are shown to correspond to guided wave modes with low attenuation and a significant out-of-plane polarization. The experimental radiation spectra are finally compared against those obtained from time transient finite element simulations that leverage geometric models reconstructed from microcomputed tomographic scans.*

Keywords: guided waves; transcranial ultrasound; parameter identification; modal analysis; vibration

## INTRODUCTION

Literature of the human skull and head dynamics and vibration began forming in the 1950s, with some of the first experimental studies focused on characterization of the mechanical impedance [1–3]. Khalil and Viano [4] were the first to identify

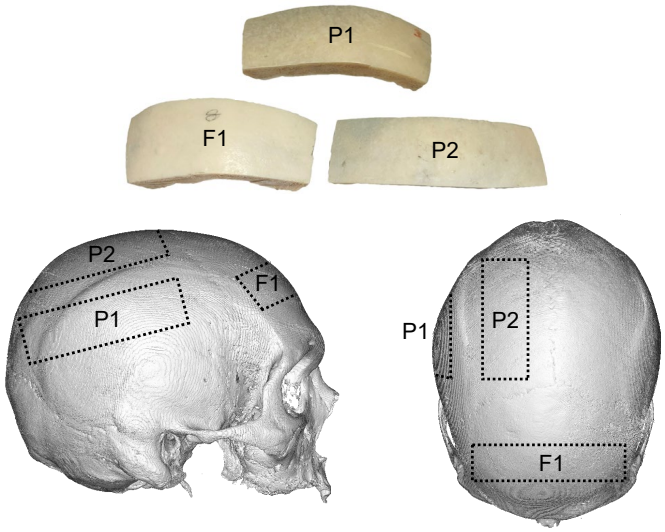


**FIGURE 1**. The skull segments considered in this study and their approximate locations on the human skull.

radiation from the human cranium. In the first track, skull segments from the parietal and frontal bone (Fig. 1) are tested in the audio-frequency regime to obtain the first handful of modal frequencies, mode shapes, and damping ratios. The methods and results are discussed in more detail by Kohtanen et al. [21]. These experimental results are then combined with layered finite element models of the segments in an iterative parameter identification scheme to obtain the isotropic elastic properties for the cortical tables and the diploë. In the second track, the cranial

## ELASTIC PARAMETER IDENTIFICATION

Here, the numerical and experimental methods for extracting elastic parameters of cortical bone and diploë are described. The process consists of first constructing a model of the cranial bone segments using a $\mu$CT scan based routine. Together with experimental modal frequencies obtained from vibration tests, the models are then used in an iterative optimization scheme that identifies the elastic parameters that minimize the difference between the experimental and numerical natural frequencies.

Cranial bone is a three-layered sandwich structure consisting of the compact inner and outer cortical tables, and the porous diploë, which has considerably different effective material properties than those of the cortical tables. For this reason, it is intuitive to consider a layered model in which the inner layer and the adjacent regions employ different sets of material properties. To this end, a numerical model that faithfully captures the boundaries between the bone layers is constructed using a combina-

tion of MATLAB's image processing toolbox [22] and COMSOL Multiphysics 5.5 [23].

First, micro-computed tomographic ($\mu$CT) scan images of a bone segment are obtained from an 87 year old human skull specimen of unknown race and medical history using Scanco Medical $\mu$CT 50 scanner at 49.6 $\mu$m resolution. The model construction algorithm begins by identifying the outline of the skull segment, from which the inner and outer boundaries are isolated using corner coordinates. The boundaries are then divided into uniformly-spaced sets of points. From each point on a boundary, the algorithm marches towards the opposite side until a gray scale value below threshold is encountered, indicating that the coordinates correspond to a cortical table–diploë boundary. The matched points are then filtered to attenuate local noise using a Savitzky-Golay filter [24] that fits subsets of adjacent points to a second order polynomial, generating two smooth curves that separate the diploë and the cortical tables. This procedure is repeated for each scan image. The identified overall outline of the bone segment, as well as the cortical table–diploë boundary coordinates are then imported into COMSOL Multiphysics 5.5 [23]. The overall closed outline of the bone segment is lofted using COMSOL design module to generate the solid geometry, whereas the open cortical table–diploë boundaries are lofted to create two surfaces that divide the solid into its constituent layers. A comparison between a bone segment and the finished numeri

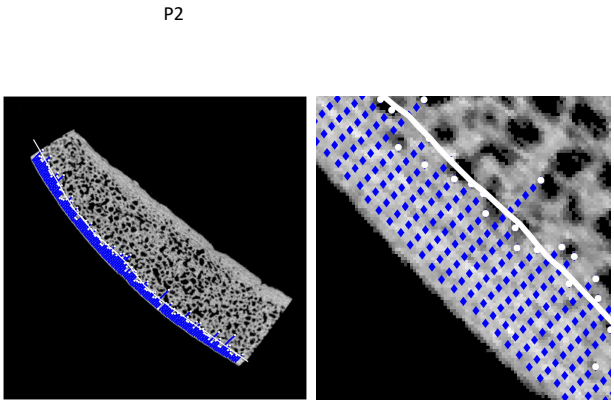


**FIGURE 2**. Inner cortical table–diploë boundary identification on a sample scan image of bone segment P2. The marching steps (blue diamonds), identified cortical table–diploë boundary points (filled white circles), and the filtered boundary line (white) are indicated.

Next, experiments conducted to identify modal frequencies, damping ratios, and mode shapes of the bone segments are described. To avoid the mass loading inherent to traditional contact excitation methods, a speaker is used to acoustically excite the bone segments, which are placed on foam to emulate free conditions. The segments are asymmetrically placed in the speaker's near-field to improve excitation of asymmetric modes

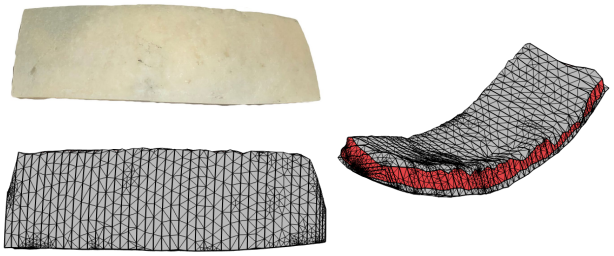

**FIGURE 3**. Skull segment P2 and its corresponding finite element mesh.

and to maximize the signal-to-noise ratio. The schematic of the experimental setup is shown in Fig. 4. Using a signal generator with data acquisition system and software included in the scanning laser Doppler vibrometer (Polytec PSV-500) system, a noise burst with frequency content in the auditory range (1-20 kHz) is sent to a speaker (Klipsch RP-400M) through a power amplifier (QSC PLX1602). The velocity measurement is triggered internally and is obtained at approximately 100 points with the scanning laser Doppler vibrometer using 10 averages. The laser software automatically converts the time-domain measurements into FRFs, which represent a transfer function between the surface velocity and the excitation voltage signal. The FRFs are then converted from velocity/voltage to velocity/pressure using free field pressure measured with a microphone at the location of the bone segment. A sample FRF is reported in Fig. 5 where the mode shapes corresponding to the most prominent resonance peaks are also shown. Lastly, it is noted that retroreflective tape is used on the bone surface to improve the laser signal-to-noise-ratio. However, due to the surface geometry of the bone, at certain measurement points the tape adheres poorly. For this reason, measurement points with coherence values less than 0.95 are excluded from the mode shape construction. After the removal of noisy measurement points, on average more than 80 points remain for evaluation of the mode shapes, which is sufficient to capture the first handful of bone segment modes as seen in Fig. 5.

Next, the methods used to identify the material properties are described. The Poisson's ratio of the cortical tables and the diploë are assumed as constants in similar vein to other modal frequency-based parameter identification efforts in bone [25], because the modal frequencies are observed to exhibit insensitivity to Poisson's ratio. The Poisson's ratios are set to $\nu_c = 0.25$ and $\nu_d = 0.10$ in close accordance with those used in the literature (see, e.g. [26,27]). The cortical and diploë densities $\rho_c$ and $\rho_d$ of a given skull segment are calculated using an expression relating the total measured bone mass to the total numerical mass estimated for the reconstructed cortical bone and diploë layers. Additionally, because density is linearly proportional to Hounsfield Unit (HU) in the $\mu$CT scans, the ratio between the cortical and diploë densities is linearly related to the corresponding average HU ratio $(HU_c/HU_d)$ in the bone regions. The expressions for

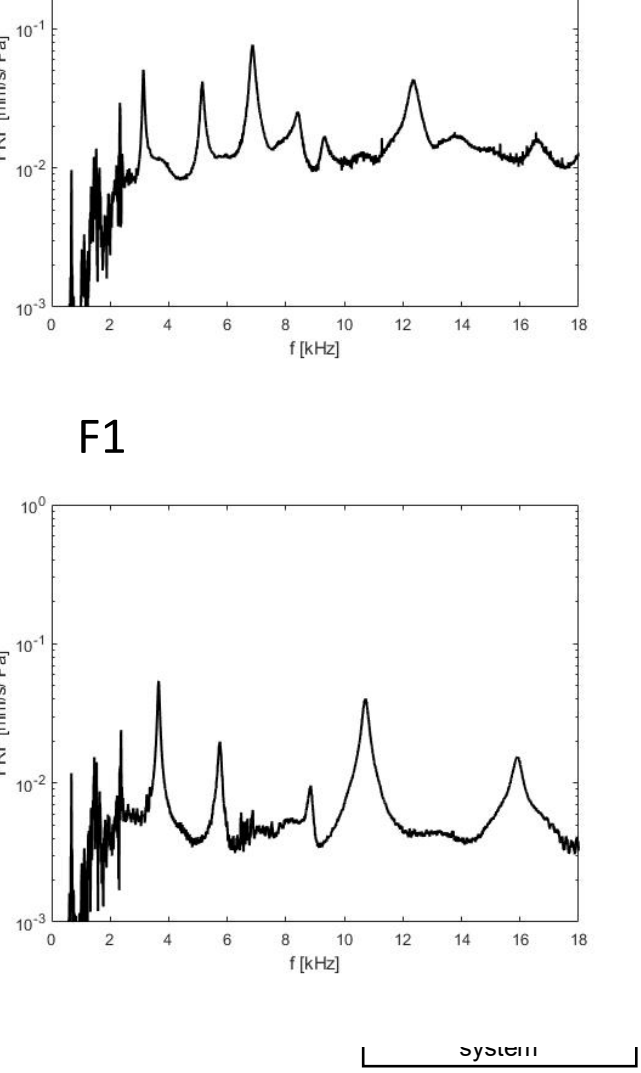


**FIGURE 4**. The experimental setup used for frequency response measurement and modal parameter extraction.

equal numerical and experimental mass, and for linear relation between density and $HU$ are stated as

$$\rho_c V_c + \rho_d V_d = m_{exp}, \tag{1}$$

$$\rho_c/\rho_d = HU_c/HU_d, \tag{2}$$

where $V_{c,d}$ are the numerically reconstructed cortical and diploë volumes, and $m_{exp}$ is the measured total mass of the bone segment. The densities $\rho_c$ and $\rho_d$ are obtained directly from Eqs. (2) and (1).

The Young's modulus of the cortical bone ($E_c$) and the diploë ($E_d$) are obtained from an optimization procedure. The procedure is based on the trust-region Gauss-Newton method described in [17, 28, 29] and seeks to iteratively minimize the functional

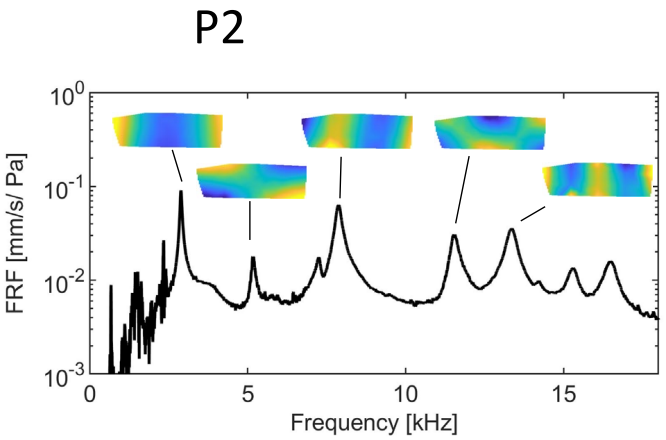


**FIGURE 5**. The average FRF across all measurement points for a sample skull segment (P2). The experimental mode shapes used in the parameter identification scheme are shown.

$$\mathscr{F}(\mathbf{E}) = \beta \, \|\mathbf{r}(\mathbf{E})\|^2 \, (\|\delta\mathbf{E}\|^2 + \gamma), \tag{3}$$

where $\mathbf{E} = \{E_c, E_d\}^{\mathrm{T}}$ is the vector of unknown elastic moduli, $\delta\mathbf{E}$ indicates the variation of $\mathbf{E}$ between two iterations, $\beta$ and $\gamma$ are penalty parameters that depend on the size of the trust region and the admissible physical bounds for $\mathbf{E}$ [28], while $\mathbf{r}(\mathbf{E}) = \{.., \omega_i^2(\mathbf{E})/\tilde{\omega}_i^2 - 1, ..\}^{\mathrm{T}}$ is the residual to be minimized, in which $\tilde{\omega}_i$ denotes the $i$th experimental frequency and $\omega_i(\mathbf{E})$ its numerical counterpart. The latter is determined from a standard finite element eigenvalue problem of the form

$$[\mathbf{K}(\mathbf{E}) - \omega^2\mathbf{M}]\mathbf{Q} = \mathbf{0}, \tag{4}$$

in which the stiffness ($\mathbf{K}(\mathbf{E})$) and mass ($\mathbf{M}$) matrices are built upon a finite element mesh of the reconstructed bone geometry.

The densities and Young's moduli obtained from the parameter identification scheme are shown in Table 1 along with average layer thickness for each cranial bone segment. With these material properties, the numerical modal frequencies are listed along with the experimental ones, their error, the experimental damping ratio, and the modal assurance criterion (MAC) values in Table 2. The damping ratios are extracted using the classical half-power point method [30] and are on the order of 2%, which are in agreement with the values found in other works for skull bone [6, 7]. Additionally, the MAC values are above 0.9 for most modes with the full MAC matrices displayed in Fig. 6. Note that the experimental and numerical mode numbers do not agree past a certain mode, because weakly excited experimental modes are excluded from the analysis, resulting in an offset between the experimental and numerical mode numbers. Sample experimental

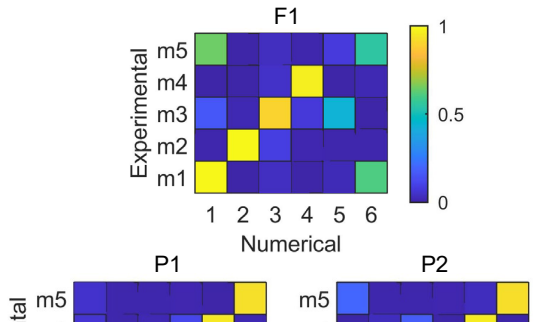


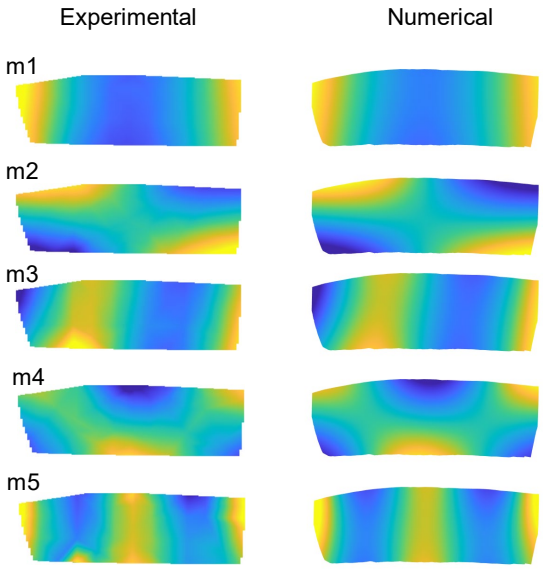


**FIGURE 7**. Representative experimental and numerical mode shapes used in the parameter identification scheme (P2).

## TRANSCRANIAL RADIATION OF GUIDED WAVES

The guided Lamb wave radiation from cranial bone to a surrounding fluid medium is analyzed by means of submersed experiments in a water tank setup, as well as a combination of numerical tools including time transient finite element simulations in COMSOL to emulate the experiments and a semi-analytical finite element (SAFE) model to generate the guided wave dispersion branches.

The experimental setup and the coordinate convention to follow can be seen in Fig. 8. The degassed cranial bone segments are submersed and excited with an ultrasonic immersion transducer (Olympus V391-SU with center frequency 0.47 MHz and -6 dB bandwidth of 61.5%) that is fed a two-and-a-half period sine burst centered at 500 kHz using an arbitrary signal generator (HP 33120A) and a power amplifier (Khron-Hite 7500). On the other side of the bone, a needle hydrophone (Teledyne Reson TC 4038), connected to a pre-amplifier (Stanford Research Systems SR560) and placed at mid-width of the bone, measures the pressure time histories $p(x,y,t)$ in a rectangular area of dimensions 40 mm–50 mm (depending on the bone segment). The spatial step of 0.25 mm provides more than ten measurement points per wavelength for the highest frequency of interest (800 kHz) for which the wavelength in water is roughly 3 mm. Representative pressure fields at different time instants for segment P1 are shown in Fig. 9. The direct wave is observed on the upper-left side of the pressure field, whereas lower amplitude wavefronts associated with leaky guided waves are seen closer to the bone.

The experimental radiation angles are obtained by first applying a Tukey window to the spatial and temporal signals. Then, taking the Fourier transform of the pressure time histories in both space and time, $\hat{p}(k_x,k_y,f) = \mathscr{F}(p(x,y,t))$, $\hat{p}$ can be inspected as a function of the two orthogonal wavenumbers $k_x$ and $k_y$ at a given frequency $f$. The pressure amplitude is non-zero in the first quadrant of the $(k_x(f),k_y(f))$ plane, for which the wavenumbers fall on the quarter circle given by $k_f(f) = \sqrt{k_x(f)^2 + k_y(f)^2}$, where $k_f(f) = 2\pi f/c_f$ is the known total wavenumber in water (density $\rho_f = 1000\,\text{kg/m}^3$, bulk wave speed $c_f = 1480$ m/s). The radiation angle $\theta$ is measured with respect to the normal to the bone surface as $tan(\theta) = k_x/k_y$. Note that, to improve the precision of the experimental radiation angles, the bone segments are positioned such that the scan area is behind a relatively flat region of the bone for which the surface normal does not vary significantly and corresponds approximately to the $y$-axis, as seen in Fig. 8.

The radiation angles are also analyzed with time transient finite element simulations in COMSOL using a phase field approach. This approach employs a $\mu$CT scan image as the computational domain. For each bone segment, the $\mu$CT scan image is obtained at mid-width of the bone and converted to binary as seen in Fig. 10. The binary structure of the image is defined through the field variable $\phi$. The white regions in the image

**TABLE 1**. Equivalent cortical table and diploë thicknesses obtained from $\mu$CT scans and converged material properties.

| Segment | Inner cortical | | | Diploë | | | Outer cortical | | |
|---|---|---|---|---|---|---|---|---|---|
| | t [mm] | E [GPa] | $\rho$ [kg/m$^3$] | t [mm] | E [GPa] | $\rho$ [kg/m$^3$] | t [mm] | E [GPa] | $\rho$ [kg/m$^3$] |
| P1 | 1.446 | 18.73 | 2165 | 6.633 | 4.35 | 1237 | 1.662 | 18.73 | 2165 |
| P2 | 1.382 | 14.70 | 1944 | 7.218 | 5.70 | 1211 | 1.546 | 14.70 | 1944 |
| F1 | 1.365 | 14.17 | 1926 | 8.090 | 5.00 | 1246 | 1.409 | 14.17 | 1926 |

**TABLE 2**. The experimental and numerical modal frequencies, their errors, the experimental damping ratios, and MAC values.

| Skull Segment | Mode ID | $f_{exp}[Hz]$ | $f_{num}[Hz]$ | Error [%] | $\zeta[\%]$ | MAC |
|---|---|---|---|---|---|---|
| P1 | m1 | 3484 | 3452 | 0.9 | 1.7 | 0.986 |
| | m2 | 5109 | 5242 | 2.6 | 1.8 | 0.996 |
| | m3 | 8097 | 7959 | 1.7 | 1.9 | 0.916 |
| | m4 | 10825 | 10848 | 0.2 | 1.8 | 0.948 |
| | m5 | 14597 | 14540 | 0.4 | 2.1 | 0.928 |
| P2 | m1 | 2891 | 2913 | 0.8 | 1.6 | 0.976 |
| | m2 | 5159 | 5193 | 0.7 | 2.2 | 0.937 |
| | m3 | 7872 | 7822 | 0.6 | 2.0 | 0.969 |
| | m4 | 11519 | 11472 | 0.4 | 1.9 | 0.958 |
| | m5 | 13359 | 13321 | 0.3 | 2.0 | 0.923 |
| F1 | m1 | 3656 | 3807 | 4.1 | 1.6 | 0.988 |
| | m2 | 5747 | 5729 | 0.3 | 1.9 | 0.987 |
| | [illegible] | [illegible] | [illegible] | [illegible] | [illegible] | [illegible] |

$$\phi(\rho_c \mathbf{u}_{tt} + \nabla \cdot \sigma(\mathbf{u})) + (1-\phi)[\rho_f(\mathbf{u}_{tt} - c_f^2 \nabla(\nabla \cdot \mathbf{u}))] = \mathbf{f}(t), \quad (5)$$

where $\mathbf{u}(t) = \{u_x, u_y\}^{\mathrm{T}}$ is the displacement field at any point $(x,y)$ of the domain, $\sigma(\mathbf{u}) = \{\sigma_{xx}, \sigma_{yy}, \sigma_{xy}\}^{\mathrm{T}}$ denotes the stress field in the bone region and $\mathbf{f}(t) = \{f_x, f_y\}^{\mathrm{T}}$ indicates an external volume force (acoustic source). Eq. (5) is defined over a finite element mesh of 6-node quadratic elements whose maximum size is approximately equal to 1/5 of the minimum significant size of the pores (in the bone region) or $c_f/(10f)$ (in the fluid region). Sample snapshots of the pressure field are observed in Fig. 11.

The semi-analytical finite element (SAFE) model [33–35] is employed to compute the radiation angle dispersion spectra. In short, the cranial bone is idealized as an infinite layered plate loaded on both sides by a water medium. A similar approach has been previously used to study the propagation characteristics of cranial Lamb waves in human skulls [14–16, 36] and in 3D printed skull phantoms [37]. The SAFE approach uses the equivalent layer thicknesses and the material properties shown in Table 1 to calculate the dispersion relation $k_x(f)$ of the skull

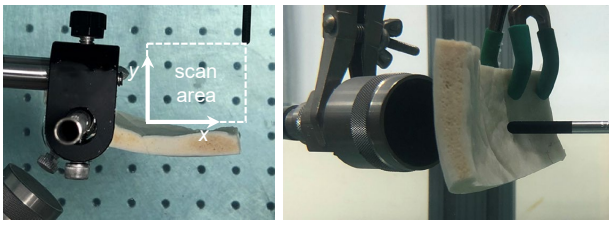


**FIGURE 8**. Experimental setup for pressure field scans.

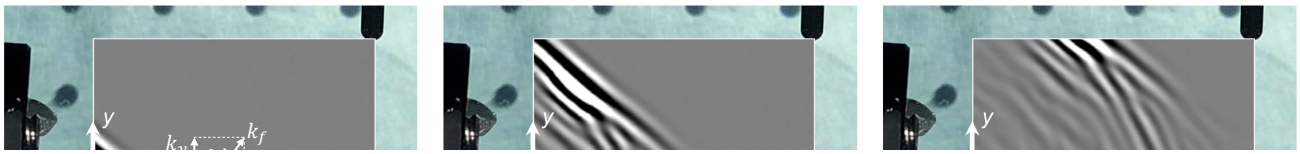


P2

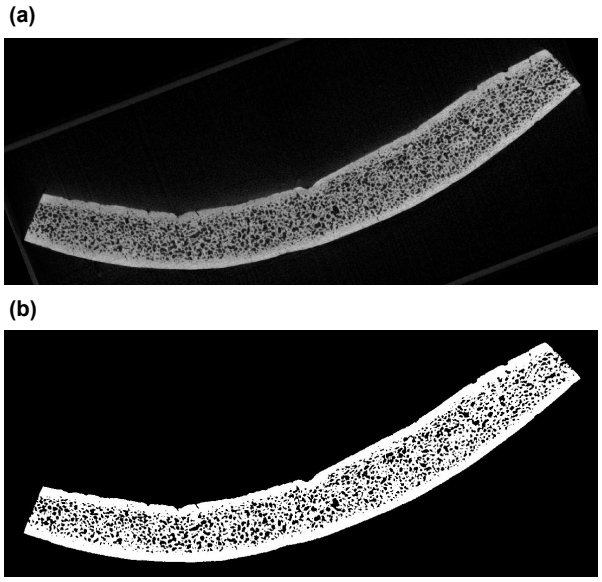


**FIGURE 10**. (**a**) Sample original $\mu$CT scan image of segment P2 obtained with 49.6 $\mu$m resolution. (**b**) The binary version of the image used in time transient simulations.

segment. This is found from a sixth-order polynomial eigenvalue problem of the form

$$\left[\sum_{i=0}^{6} \gamma^i(k_x(f))\mathbf{A}_i(f)\right]\mathbf{U}(k_x(f)) = \mathbf{0}. \tag{6}$$

The derivation of Eq. (6) and the operators $\mathbf{A}_i(f)$ $(i = 0,...,6)$ are given in [20]. The eigenvalues $\gamma(k_x(f))$ in Eq. (6) are computed by linearizing the system in state space and applying standard eigenvalue solvers. The complex Lamb wavenumbers are postprocessed for a given frequency as $k_x(f) = k_f(f)[\gamma(f) + \gamma^{-1}(f)]/2$. Using the generalized Snell's law, the associated radiation angles $\theta(k_x(f))$ are obtained from the relation

$$\theta(k_x(f)) = \sin^{-1}\left[\frac{\mathrm{Re}(k_x(f))}{k_f(f)}\right]. \tag{7}$$

The radiation angle dispersion branches obtained with SAFE are overlaid with the experimental radiation angles in Fig. 12, with zero degrees indicating normal to bone surface. SAFE points with a high attenuation (more than 500 Np/m) and high wavelength (greater than 2.5 cm) have been removed as these modes are not experimentally captured due high spatial decay rates and large wavelength-to-thickness ratios. Furthermore, the SAFE result is color-coded based on the wave polarization; i.e., high out-of-plane polarization (strong bone-to-fluid coupling) is shown with dark color. The maximum experimental pressure amplitude is normalized to one at each frequency. Although it is difficult to tell apart which particular guided wave mode is leaking energy at a given frequency, the experimental dispersion spectra are accompanied by corresponding SAFE dispersion branches particularly in the 250–750 kHz range with high SNR. The guided wave dispersion branches that accompany the experimental results predominantly correspond to modes with at least a moderate out-of-plane displacement polarization and low attenuation.

In addition to the experiments, the SAFE dispersion branches are also overlaid with the time transient finite element result in Fig. 13 obtained with the same procedure as that described for the experimental radiation angles. Similar to the experimental results, a given dispersion contour tends to be accompanied by a corresponding SAFE dispersion branch for highly excited frequencies. It is worth to note that for both the experimental and time transient result, the radiation angle is highly frequency-dependent in particular near 50–150 kHz. The radiation angles obtained from time transient simulations are similar, but not identical to the experimental ones for a few reasons. First, the simulations consider a 2D plane strain condition, whereas in reality the bone segments have a finite depth and the pores have

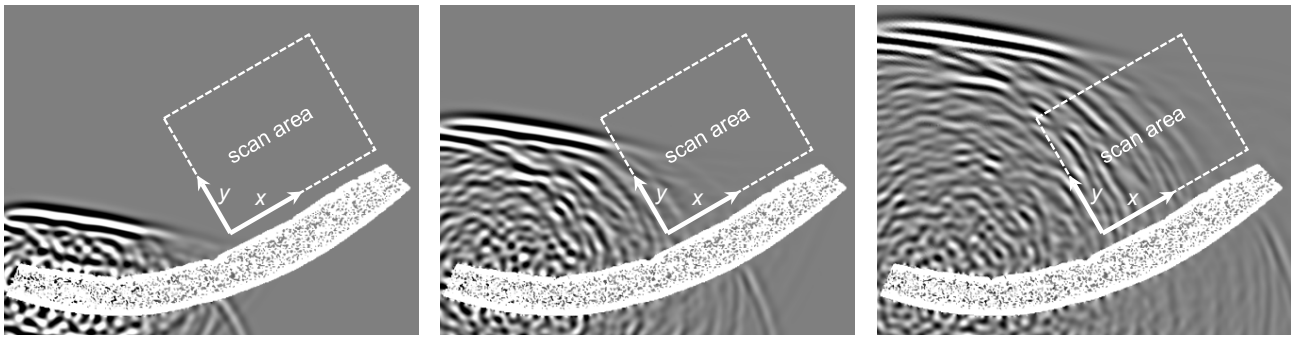


**FIGURE 11**. Snapshots of the time transient finite element pressure field at different time instants for segment P2.

a sphere-like geometry. Thus, the time transient results may exaggerate the effect of pores. Secondly, any material damping present in the cranial bone is not considered in the simulations, so modes that are damped out in the experiments may still be present in the time transient dispersion spectra.

## CONCLUSIONS

In the first track of this work, the elastic parameters of the cortical tables and the diploë are extracted for several cranial bone segments using an iterative parameter identification scheme that leverages high-fidelity numerical models and experimental vibration results by minimizing the difference between the corresponding natural frequencies. The numerical models are constructed using a $\mu$CT scan-based image reconstruction scheme that yields separate cortical table and diploë domains that are modeled with different isotropic elastic parameters. The vibration experiments are performed in free conditions using a speaker as the excitation source to avoid mass-loading the light bone segments. After the parameter identification scheme, the converged numerical natural frequencies and mode shapes are in good agreement with the experimental results (1.6% error in frequencies, average modal assurance criterion 0.93).

In the second track, the focus is switched to higher frequency (up to 800 kHz) wave propagation behavior in the bone segments. In this frequency regime, various guided Lamb wave modes propagate in the bone. Furthermore, when the bone is submersed in water, these modes can leak energy into the surrounding fluid medium. To study the radiation of guided waves, the bone segments are degassed, submersed, and excited with an ultrasonic transducer placed in front of the outer cortical table. The pressure time histories in the fluid medium on the other side of the bone segment are then measured and analyzed to find the experimental radiation angle dispersion spectra, which are shown to closely follow the predicted guided Lamb wave dispersion branches obtained from fluid-loaded layered semi-analytical finite element method using the material properties identified in the first track. The results indicate that the radiated energy is highly frequency-dependent in the 50–150 kHz regime, and that the radiated energy at a given frequency originates from guided wave modes with low attenuation and high out-of-plane polarization. The experimental observations are reproduced using pressure fields generated with a time transient finite element model.

These results pave way to adapting leaky guided waves as an alternative to conventional transcranial transmission techniques. While conventional focused ultrasound is limited in its treatment envelope to the central region of the brain, guided Lamb wave-based ultrasound could be used to efficiently access more remote brain regions [19]. The results shown herein are a fundamental investigation of cranial bone radiation characteristics that serve as a foundation for leveraging guided cranial waves for transcranial ultrasound.

## ACKNOWLEDGMENT

This work was supported by the NSF grant (CMMI Award No. 1933158) on Coupling Skull-Brain Vibroacoustics and Ultrasound Toward Enhanced Imaging, Diagnosis, and Therapy.

## REFERENCES

[1] Franke, E. K., 1956. "Response of the human skull to mechanical vibrations". *The Journal of the Acoustical Society of America,* ***28***(6), pp. 1277–1284.

[2] Hodgson, V., Gurdjian, E., and Thomas, L., 1967. "The determination of response characteristics of the head with emphasis on mechanical impedance techniques". In 11th Stapp car crash conference, no. 670911.

[3] Stalnaker, R. L., Fogle, J. L., and McElhaney, J. H., 1971. "Driving point impedance characteristics of the head". *Journal of Biomechanics,* ***4***(2), pp. 127–139.

[4] Khalil, T. B., Viano, D., and Smith, D., 1979. "Experimental analysis of the vibrational characteristics of the human skull". *Journal of Sound and Vibration,* ***63***(3), pp. 351–376.

[5] McKnight, C. L., Doman, D. A., Brown, J. A., Bance, M.,

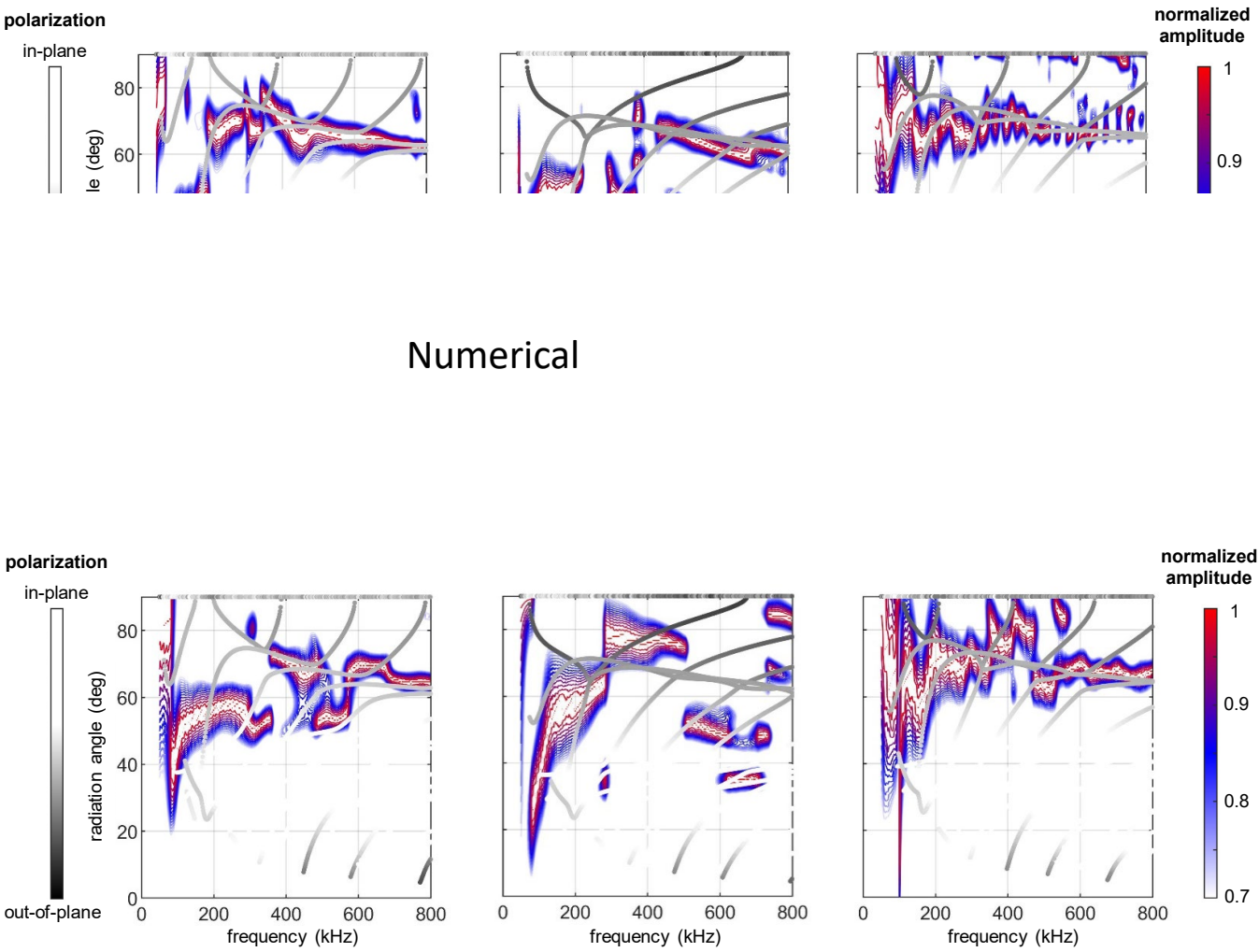


**FIGURE 13**. Time transient finite element radiation angle dispersion spectra (contours) overlaid with the dispersion branches from SAFE (scatter points) for segments (**a**) P1, (**b**) P2, and (**c**) F1. Light color of the dispersion branch corresponds to predominantly in-plane polarization, whereas dark color corresponds to out-of-plane polarization. 7.5" = page width excluding margins


and Adamson, R. B., 2013. "Direct measurement of the wavelength of sound waves in the human skull". *The Journal of the Acoustical Society of America,* ***133***(1), pp. 136–145.

[6] Horácek, J., Veselỳ, J., Pešek, L., and Vohradnık, M., 2003. "Fundamental dynamic characteristics of human skull". In Nat. Conf. Engineering Mechanics, pp. 12–15.

[7] Eslaminejad, A., Hosseini-Farid, M., Ziejewski, M., and Karami, G., 2020. "Constitutive properties determination of human cranium by an experimental–computational modal analysis". *Journal of Vibration and Acoustics,* ***142***(1).

[8] Håkansson, B., Brandt, A., Carlsson, P., and Tjellström, A., 1994. "Resonance frequencies of the human skull in vivo". *The Journal of the Acoustical Society of America,* ***95***(3), pp. 1474–1481.

[9] Nickell, R., and Marcal, P., 1974. "In-vacuo modal dynamic response of the human skull". *Journal of Engineering Industry*.

[10] Voo, L., Kumaresan, S., Pintar, F. A., Yoganandan, N., and Sances, A., 1996. "Finite-element models of the human head". *Medical and Biological Engineering and Computing,* ***34***(5), pp. 375–381.

[11] Tse, K. M., Tan, L. B., and Lee, H. P., 2017. "The skull and brain: Computer models for the head and its protection". In *Military Injury Biomechanics*. CRC Press, pp. 175–220.

[12] Laksari, K., Kurt, M., Babaee, H., Kleiven, S., and Camarillo, D., 2018. "Mechanistic insights into human brain im-

pact dynamics through modal analysis". *Physical review letters,* ***120***(13), p. 138101.

[13] Cotton, R., Pearce, C. W., Young, P. G., Kota, N., Leung, A., Bagchi, A., and Qidwai, S., 2016. "Development of a geometrically accurate and adaptable finite element head model for impact simulation: the naval research laboratory–simpleware head model". *Computer Methods in Biomechanics and Biomedical Engineering,* ***19***(1), pp. 101–113.

[14] Estrada, H., Gottschalk, S., Reiss, M., Neutschmelting, V., Goldbrunner, R., and Razansky, D., 2018. "Observation of guided acoustic waves in a human skull". *Ultrasound in Medicine and Biology,* ***44***(11), pp. 2388 – 2392.

[15] Estrada, H., Gottschalk, S., Reiss, M., Neuschmelting, V., Rebling, J., Goldbrunner, R., and Razansky, D., 2018. "Looking at the skull in a new light: Rayleigh-lamb waves in cranial bone". In 2018 IEEE International Ultrasonics Symposium (IUS), pp. 1–3.

[16] Sugino, C., Ruzzene, M., and Erturk, A., 2021. "Experimental and computational investigation of guided waves in a human skull". *Ultrasound in Medicine & Biology,* ***47***(3), pp. 787–798.

[17] Mazzotti, M., Sugino, C., Kohtanen, E., Erturk, A., and Ruzzene, M., 2021. "Experimental identification of high order lamb waves and estimation of the mechanical properties of a dry human skull". *Ultrasonics,* ***113***, p. 106343.

[18] Mazzotti, M., Kohtanen, E., Erturk, A., and Ruzzene, M., 2021. "Experimental and numerical analysis of lamb wave transmission through the coronal suture of a dry human skull". In Proceedings of Meetings on Acoustics, Vol. 149, pp. A42–A42.

[19] Firouzi, K., Ghanouni, P., and Khuri-Yakub, B. T., 2017. "Efficient transcranial ultrasound delivery via excitation of lamb waves: Concept and preliminary results". In 2017 IEEE International Ultrasonics Symposium (IUS), IEEE, pp. 1–4.

[20] Mazzotti, M., Kohtanen, E., Erturk, A., and Ruzzene, M., 2021. "Radiation characteristics of cranial leaky lamb waves". *IEEE Transactions on Ultrasonics, Ferroelectrics, and Frequency Control,* ***68***(6), pp. 2129–2140.

[21] Kohtanen, E., Mazzotti, M., Ruzzene, M., and Erturk, A., 2021. "Vibration-based elastic parameter identification of the diploë and cortical tables in dry cranial bones". *Journal of the Mechanical Behavior of Biomedical Materials,* under review.

[22] The MathWorks Inc., 2020. *MATLAB version 9.8.0.1451342 (R2020a)*. Natick, Massachusetts.

[23] COMSOL Inc., 2020. *COMSOL Multiphysics Reference Manual 5.5*. Stockholm, Sweden.

[24] Orfanidis, S. J., 1995. *Introduction to signal processing*. Prentice-Hall, Inc.

[25] Taylor, W., Roland, E., Ploeg, H., Hertig, D., Klabunde, R., Warner, M., Hobatho, M., Rakotomanana, L., and Clift, S., 2002. "Determination of orthotropic bone elastic constants using fea and modal analysis". *Journal of Biomechanics,* ***35***(6), pp. 767–773.

[26] Chang, Y., Kim, N., and Stenfelt, S., 2016. "The development of a whole-head human finite-element model for simulation of the transmission of bone-conducted sound". *The Journal of the Acoustical Society of America,* ***140***(3), pp. 1635–1651.

[27] Sahoo, D., Deck, C., Yoganandan, N., and Willinger, R., 2013. "Anisotropic composite human skull model and skull fracture validation against temporo-parietal skull fracture". *Journal of the Mechanical Behavior of Biomedical Materials,* ***28***, pp. 340–353.

[28] Mazzotti, M., Mao, Q., Bartoli, I., and Livadiotis, S., 2019. "A multiplicative regularized gauss-newton method with trust region sequential quadratic programming for structural model updating". *Mechanical Systems and Signal Processing,* ***131***, pp. 417 – 433.

[29] Mazzotti, M., Sugino, C., Erturk, A., and Ruzzene, M., 2020. "Matrix pencil estimation of guided waves dispersion in a human skull". In 2020 IEEE International Ultrasonics Symposium (IUS), pp. 1–3.

[30] Inman, D. J., and Singh, R. C., 1994. *Engineering vibration*, Vol. 3. Prentice Hall Englewood Cliffs, NJ.

[31] Olson, L. G., and Bathe, K.-J., 1983. "A study of displacement-based fluid finite elements for calculating frequencies of fluid and fluid-structure systems". *Nuclear Engineering and Design,* ***76***(2), pp. 137–151.

[32] Pinton, G., Aubry, J.-F., Bossy, E., Muller, M., Pernot, M., and Tanter, M., 2012. "Attenuation, scattering, and absorption of ultrasound in the skull bone". *Medical physics,* ***39***(1), pp. 299–307.

[33] Bartoli, I., Marzani, A., Lanza di Scalea, F., and Viola, E., 2006. "Modeling wave propagation in damped waveguides of arbitrary cross-section". *Journal of Sound and Vibration,* ***295***, pp. 685 – 707.

[34] Mazzotti, M., Marzani, A., Bartoli, I., and Viola, E., 2012. "Guided waves dispersion analysis for prestressed viscoelastic waveguides by means of the safe method". *International Journal of Solids and Structures,* ***49***(18), pp. 2359 – 2372.

[35] Hayashi, T., and Inoue, D., 2014. "Calculation of leaky lamb waves with a semi-analytical finite element method". *Ultrasonics,* ***54***(6), pp. 1460 – 1469.

[36] Estrada, H., Rebling, J., and Razansky, D., 2017. "Prediction and near-field observation of skull-guided acoustic waves". *Physics in Medicine and Biology,* ***62***(12), may, pp. 4728–4740.

[37] Gao, J., Chen, Q., Jiang, C., Hu, B., Zhang, J., Xu, K., and Ta, D., 2019. "A free plate model could predict ultrasonic guided waves propagation in a 3d printed skull phantom".



 

In 2019 IEEE International Ultrasonics Symposium (IUS), pp. 2031–2033.